

Phase Quantized Metasurface Supercells for Wave Manipulation and RCS Reduction

Rajanikanta Swain* and Rabindra K. Mishra

Abstract—Recently, the introduction of surface phase in Snell’s law and Huygens’ phenomena leads to ultrathin phased surfaces which can tailor the transmission and scattering of the incident wavefront in many ways. In this article, a remodeled Jerusalem cross used as the meta-element whose geometrical parameters are varied to obtain 360° phase variation and a 3-bit quantization is presented to design phase coded surfaces to manipulate (focusing and splitting) normally incident beam. Further, two 3-bit phase quantized supercells of approximately 2λ length and width are proposed and simulated (3×3 matrix arrangement) to test and compare the scattering properties with traditional chessboard type supercell. Obtained simulated results show diffused reflections for both the models and reduced intensity of four corner lobes in comparison to chessboard supercells (at $\theta = 30^\circ$ and $\phi = 45^\circ$). Experimentally recorded monostatic RCS of model-2 prototype has a close agreement with the simulated results and more than 10 dBsm RCS reduction observed from 9 GHz–11 GHz.

1. INTRODUCTION

Metal-dielectric composite of periodic/apperiodic media to manipulate electromagnetic wavefronts for desired characteristics comes under EM metamaterial [1]. They have potential applications like EM cloaks [2], negative refraction [3], focusing [4], etc. Transformation optics/electromagnetics forms the basis of synthesis and analysis of metamaterials [5]. Usually, it shows electrical anisotropy and a bulky structure. Multilayer geometry tends to be challenging for many laboratories. Loss/dispersion is high due to multi-layer geometry hence challenging to realize it practically. These drawbacks give rise to a viable mechanism known as flat optics or metasurface [6] which is the 2D counterpart of the metamaterials. These are ultrathin reflect/transmit arrays of sub-wavelength particles and based on abrupt phase variation instead of modification of propagation medium characteristics. Phase distribution of these inhomogeneous surfaces follows the principle of generalized Snell’s law [7] which is the most relevant technique to tailor the incident wavefront by employing sub-wavelength scatters. In general, the phased surfaces agree with the equivalence principle and control the tangential component of the field at sub-wavelength areas, which trigger the desired field outside the cover. Analogously, the technique to modify the wave path by phase gradient surfaces led to significant functionalities like the ultrathin flat lens [8,9], orbital angular momentum wavefront generator [10–12], polarization converter [13,14], electromagnetic cloaks [15,16], holograms [17], novel antennas [18] and many more. Also, numerical approaches for the efficient and fast design of all-dielectric metasurfaces are proposed recently [19]. Coding metamaterials and digitalization of sub-wavelength element distribution by single/multi-bit optimized sequence attracted many researchers in the recent past. Quantization of reflection/transmission phase based on its variation by changing meta-particle geometry simplified the metasurface research which led to promising applications in the area of wave manipulation [20,21],

Received 16 August 2018, Accepted 2 October 2018, Scheduled 13 October 2018

* Corresponding author: Rajanikanta Swain (swain.rajanikanta@gmail.com).

The authors are with the Department of Electronics Science, Berhampur University, India.

polarization independent scattering [22] and beam reconfiguration [23]. Digitalized surfaces based on Pancharatnam-Berry phase are also quite an effective method for reshaping the wavefront [24].

Radar Cross Section (RCS) reduction is one of the mechanisms to obtain stealth properties of an object by the theory of diffused/unusual reflections. With rapid improvements in radar research, efficient radar absorbing coats and surfaces to produce reflections in unexpected direction are necessary for national defense applications. Conventionally in stealth technology, the geometry of objects was optimized to obtain low backscattered waves [25], and ferrite-based screens and pyramidal absorbers [26] are widely used as viable agents to suppress RCS, but are too bulky for practical installation over moving objects at low frequencies. Frequency Selective Surfaces (FSS) [27] and surface plasmons for modifying the incident beam polarization [28] can also be used for controlling RCS, but these techniques suffer from narrow bandwidth and multiple scan angle issues. Later, to reduce structural dimension and achieve low reflections by transforming incident beam energy to heat using sub-wavelength meta-element based surface/medium is proposed [29, 30]. Also, investigations show two sets of supercells made up of an artificial magnetic conductor (AMC) and perfect electric conductors (PEC) surfaces with 180° phase difference used to design chessboard-like surface to reduce RCS [31, 32]. Chessboard surface consists of two separate AMC supercells is also proposed [33–35] to achieve wider bandwidth than the previous one. In both the designs the backscattered beam in the normal direction is suppressed enough, but the incident energy diagonally reflects into four quadrants with high intensities and acts as a resonance surface with narrow operating frequencies. Therefore, more than 70% fractional bandwidth of 10 dBsm RCS reduction can be achieved by a chessboard surface, while reduction of the maximum reflection intensity is still a challenge. In a few articles, complex optimization based phased distributions are obtained to design randomly phased polarization independent surface to reduce RCS [36, 37] with fractional bandwidth more than 90% at $\theta = \phi = 0^\circ$ plane while ignoring anomalously scattering beams.

In this work, a remodeled Jerusalem cross meta-element is used to achieve 360° phase variation to avoid drawbacks in square/circular patch type conventional reflectarray elements [38] where a steep slope is obtained while plotting size variation versus reflection phase. A hybrid meta-element consists of a ring, and four t-type stubs are used to obtain quasi-linear phase response. The concept of phase quantization is introduced, and based on that planar surfaces are proposed and simulated to obtain wave manipulation applications like beam splitting and focusing. Further two supercells are intended to manipulate backscattered RCS and reflection efficiency, and 3×3 supercell based phased surfaces are designed and simulated. Simulated results are compared with conventional chessboard type supercells and copper plates. Simulated 3D RCS patterns are displayed to strengthen the proposed method to reduce maximum reflection efficiency. Further, 2D results are given to compare the two models with a chessboard, copper plate at $\theta = \phi = 0^\circ$ and $\theta = 30^\circ$, $\phi = 45^\circ$. The fabricated prototype of model-2 (with high diffusion capabilities) tested for monostatic RCS, and the results agree with 10 dBsm reduction of backscattered intensity from 9 GHz to 11 GHz.

2. META-ATOM SYNTHESIS AND WAVE MANIPULATION USING QUANTIZED SURFACES

Conventionally, to obtain the desired phase profile at the reflectarray/metasurface front panel, researchers use patches, loops, crosses, and dipole type sub-wavelength meta-particles. Insufficient bandwidth, less than 360° phase response and a steep phase versus element variation curve are the major drawbacks of meta-elements mentioned above which reduces the operational bandwidth of the reflector and also leads to fabrication difficulties. The depiction in Figure 1(a) displays a remodeled Jerusalem cross where a quasi-linear phase response is obtained due to compact size and placement of four T-type stubs around the ring whose resonant frequencies are placed closely within the desired band. Multiple resonances from the stubs and the ring merged into a single resonance with almost maximum reflection efficiency. The structure on top and metallic ground with thickness 0.02 mm make a sandwich geometry with a low-cost FR4 substrate having dielectric constant 4.3 and thickness 1.6 mm at the middle. Printed geometry of the meta-particle has width $w = 0.3$ mm, periodicity $p = 7$ mm, and the variable parameter ‘ l ’ is used to control the reflection coefficient.

A set of simulations of meta-particles is performed with university license of CST Microwave StudioTM EM-package. Unit-cell boundary conditions of Microwave studio in x - and y -directions, an

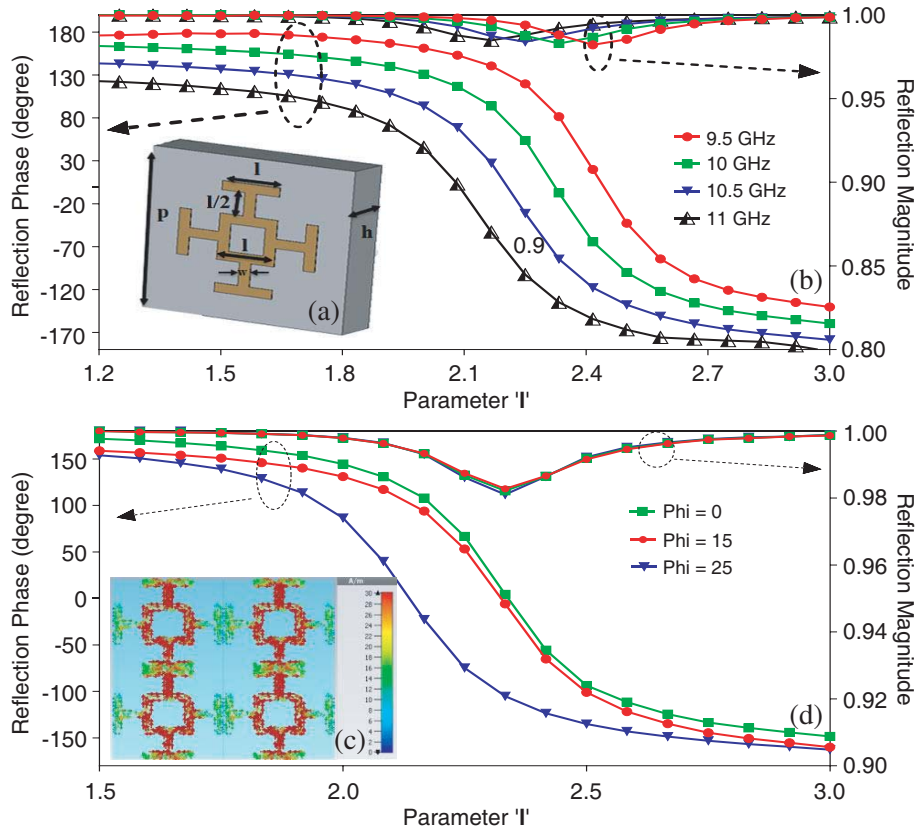


Figure 1. (a) The geometry of the meta-element, (b) phase and amplitude of reflection for different frequency samples, (c) the surface current and (d) phase and amplitude of reflection for several angles of incidence.

x/y -polarized plane wave port at z -directions, tetrahedral meshing with minimum and maximum edge length of 0.004 mm and 2.5 mm are used in frequency domain platform to accomplish the full wave performance. The parameter ‘ l ’ was varied from 1 mm to 3 mm in inbuilt optimization toolbox to obtain the desired phase and amplitude response of the meta-element. Figure 1(b) shows the recorded phase and amplitude responses at four different frequency samples to strengthen the broadband functionality of the meta-particle. Approximately 340° variation is observed at all frequency samples with the change in the ring and stub size; we also observed maximum reflection magnitude at all taken samples which proves the meta-element as a perfect reflector. The surface current displayed in Figure 1(c) clears the role of the center ring which increases the current path within the same unitcell dimension which minimizes the meta-atom size and reduces the mutual coupling between adjacent cells. To study and analyze the functionalities of the proposed meta-element as an agent to design asymptotic conformal surfaces, we studied the phase and amplitude responses with three different incident angles (0° , 15° , and 25° degrees). As depicted in Figure 1(d), the meta-element gives the same phase response of 360° for variation in parameter ‘ l ’ from 1.6 mm to 3 mm while keeping the magnitude of the reflection amplitude close to unity, which strengthens the argument that the meta-element can also be used for conformal surfaces with an incident angle tolerance of more than 25° . From above experiments, it is clear that the phase response is quasi-linear instead of a steep curve (in common cases), which will help us to find the respective phase values for change in meta-element parameter and design novel reflectors with better functionalities.

The approach of digital elements or codifications of meta-elements according to their phase response which describes behaviors of metamaterial or metasurface is an advantage over effective medium based complex calculations [18–21]. Implementation of binary codes to represent single/multi-bit elements based on reflection phase discretization can simplify the element distribution over phased reflecting

surfaces. In our case, manipulation of scattered wavefront based on the coded phased surface is realized and implemented to perform RCS reduction. A 3-bit quantization method is proposed to codify the reflection phase which discretizes the element parameter ‘l’ values to obtain a suitable reflection phase as shown in Figure 2. The phase response of the meta-element at 10 GHz is divided into eight parts to assign proper element size which can be utilized to design anisotropic phased reflective surfaces to perform novel functionalities.

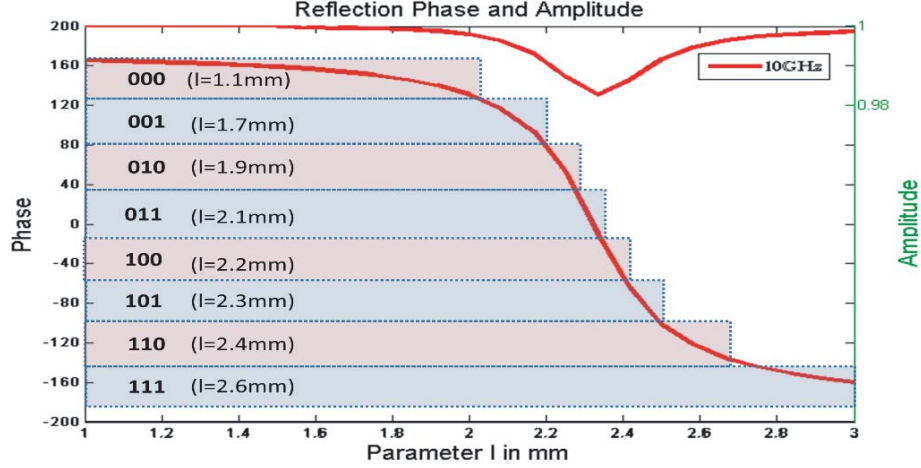


Figure 2. Quantization of meta-element phase and the corresponding physical length of the tuning parameter.

At the first stage of our experiment, we design and simulate two planar phase coded surfaces to validate its operation as an electromagnetic beam splitter and in-plane focusing flat-lens. Two printed flat-surfaces are designed by proper arrangement of above-studied meta-element along the horizontal axis (x -axis). For the beam collimator surface (for focusing), the coded surface has a 3-bit variation sequence (16-elements) starting from **000** to **111** to **000**, while the beam splitting metasurface has a series **111** to **000** to **111** along the x -axis. Two 8×16 element surfaces are designed keeping the surface symmetric along y -axis and simulated using time-domain solver of CST Microwave Studio with 12 hexahedral meshes per wavelength, and a linearly polarized plane wave is projected perpendicularly towards the phase coded surface. The scattered wavefront is studied for four discrete frequency samples (9.5 GHz, 10 GHz, 10.5 GHz, and 11 GHz) as displayed in Figure 3. These reflected waves obey Equation (1) for generalized Snell’s law of reflection [7] of plane waves.

$$n \sin \theta_r - n \sin \theta_i = \frac{1}{k_0} \frac{d\varphi}{dx} \quad (1)$$

$$n \sin \theta_r - n \sin \theta_i = \frac{\lambda}{2\pi} \frac{d\varphi}{dx} \quad (2)$$

Here θ_r represents the angle of reflection, dx the period of the meta-atom spacing, $d\varphi$ the phase variation between adjacent meta-atoms, and λ the free space wavelength. Considering a normally projected plane-wave in free-space towards the phased surface with a periodicity of $\lambda/8$ and a phase variation of $\pi/4$ between consecutive elements, we will obtain a reflection angle of 29° at 11 GHz.

From scattered E -fields shown in Figure 3, it is clear that the PEC plate redirects the incident field in normal direction while coded phase sequenced surfaces divert the beam making an angle with the incident plane. The reflection angle depends on the phase difference between two consecutive meta-elements in the array and the variation along the horizontal axis. From the comparisons of full-wave simulation results displayed in Figure 3, we can observe powerful manipulation of electromagnetic wavefront using coded planar phased surfaces as a beam splitter and focusing application. The principle of quantization of reflection phase can further be utilized to design surfaces with better functionalities for X-band wireless communication.

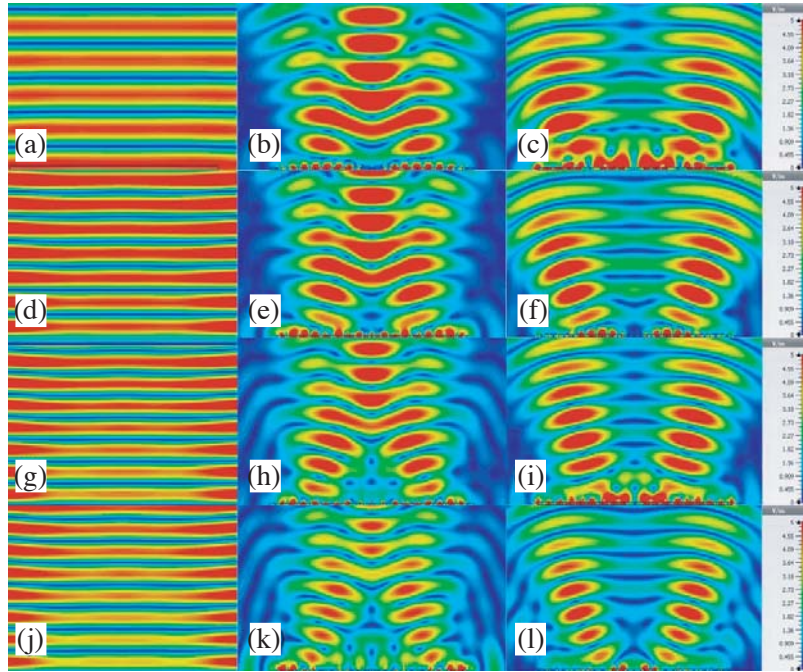


Figure 3. Scattered E -field from (a), (d), (g) & (j) PEC plate, (b), (e), (h) & (k) phase-quantized beam collimator surface, (c), (f), (I) & (l) phase-quantized beam splitting surface for a normal incident of plane-wave at 9.5 GHz, 10 GHz, 10.5 GHz and 11 GHz.

3. ANALYSIS OF PHASE QUANTIZED SUPERCELLS (PQS) TO REDUCE RCS

The working mechanism of conventional AMC chessboard supercells based on two different kinds of subwavelength sections with 180° phase difference which suppresses the backscattered beam but can be easily identified due to four high intense reflected beams. More physical insight can be given by considering the array factor from planar array theory [39], which is

$$AF(\theta, \varphi) = \sum_{m=1}^{M-1} \sum_{n=1}^{N-1} e^{j[(k\partial x \sin\theta \cos\varphi) + (k\partial y \sin\theta \sin\varphi) + (\theta(m,n))]} \quad (3)$$

Here M and N describe total element numbers along x and y coordinates; ∂x , and ∂y represent the periodicity of meta-elements along x -axis and y -axis, respectively; k is the free space wave number; $\theta(m, n)$ is the relative phase response of (m, n) th meta-element. Due to only two types of phased grids, it is easy to synthesize scattered beams using the two-element matrix in conventional planar array theory, but it is difficult to analyze theoretically when the type of phased element grids is more inside the parent rectangular supercell. As depicted in Figure 4(a), we use two meta-element sizes from 3-bit quantization of Figure 3 with 180° phase difference to construct chessboard supercell. The coded phase-mask shown in Figure 4(b) is the proposed model-1 whose eight sectors consist of coded meta-elements with 45° phase variation increasing clockwise between adjacent segments. Trying sectorized modifications, Figure 4(c) displays model-2 with eight sectors to obtain arbitrary asymmetric phase distribution by placing the phased sectors randomly throughout the parent cell.

Computer-aided designs of PQSs displayed in Figures 4(d)–(f) are used to demonstrate our models concisely by simulation. The chessboard supercells have four rectangular sectors with 36 elements in each, while model-1 and model-2 have eight sectors with 16 meta-elements each. The supercells in all three configurations have size $84\text{ mm} \times 84\text{ mm}$ and printed over a most commonly available low cost grounded FR4 substrate with dielectric constant 4.3 and thickness 1.6 mm. To validate the operating mechanism of the proposed PQSs, separate 3×3 arrangements of supercells are designed precisely using

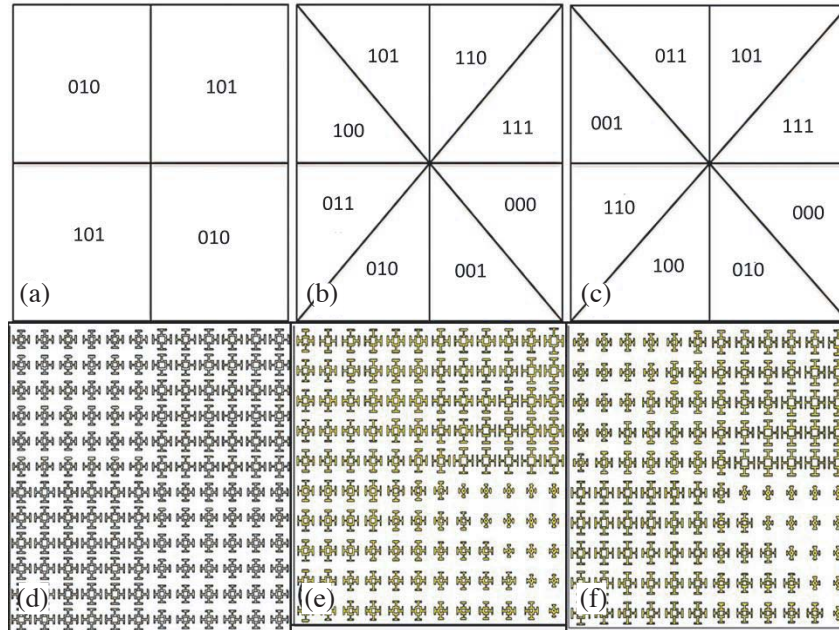


Figure 4. (a)–(c) Track wise phase distribution schemes and (d)–(f) computer-aided models of the chessboard, PQS model-1 and PQS model-2 filled with proposed meta-elements of corresponding phase value.

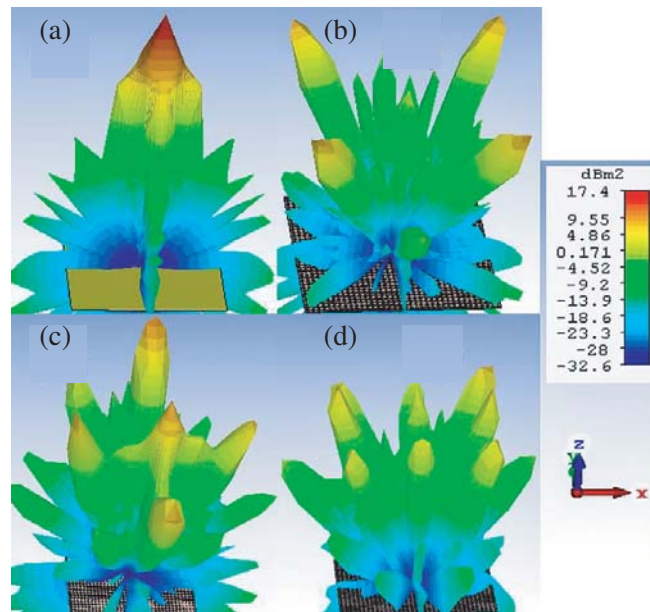


Figure 5. 3D far-field patterns at 10 GHz for (a) metal plate, (b) chessboard, (c) model-1 and (d) model-2.

CST Microwave StudioTM for each configuration with side lengths approximately $8.4\lambda_0$ (252 mm) at 10 GHz, and each model consists of 36×36 elements in xy -plane. A transient time-domain solver of CST used for full-wave analysis of the PQSs with open boundary condition and an x -polarized plane-wave is used as a source with 15 hexahedral meshes per wavelength for excellent results. Bistatic RCS along with far-field scattering patterns of three PQS configurations is calculated and compared with RCS of a copper plate having the same size. Figures 5(a)–(d) gives the scattered RCS 3D pattern of copper

plate and three designed PQSs at 10 GHz. From the intensity scale, it is clear that the maximum beam intensity in the case of the copper plate is approximately 18 dBsm, and the chessboard configuration has 8.9 dBsm with four main beams in diagonal directions.

For model-1 five main beams are laying on x -axis and y -axis with maximum intensity 8.2 dBsm, but the scattered rays in model-2 diffuse into more than nine beams in all directions and dramatically reduce the backscattering with maximum intensity 5 dBsm which is 12 dBsm less than that of the copper plate. The chessboard supercell is made by just two types of element with 180° difference in phase, while eight different phased sectors used in proposed supercell model-1 and model-2. These distributions lead to an increased number of interfaces within adjacent phased sectors and will redirect the incident beam into several scattered beams with low intensities.

Summarized results in Figure 6(a) depict the broadband RCS reading at $\varphi = 0^\circ$ plane which clearly describes that the RCS of chessboard PQS is reduced to the maximum value at 10.1 GHz and gives an average performance at other frequencies due to resonance behavior of the supercell and just two types of element phase used. RCS reduction curves in Figure 6(b) show that both model-1 and model-2 possess 10 dBsm RCS reduction throughout the band from 9.1 GHz to 11 GHz. Moreover, model-2 gives the best performance among three PQSs due to minimum 15 dBsm RCS reduction from 9.3 GHz to

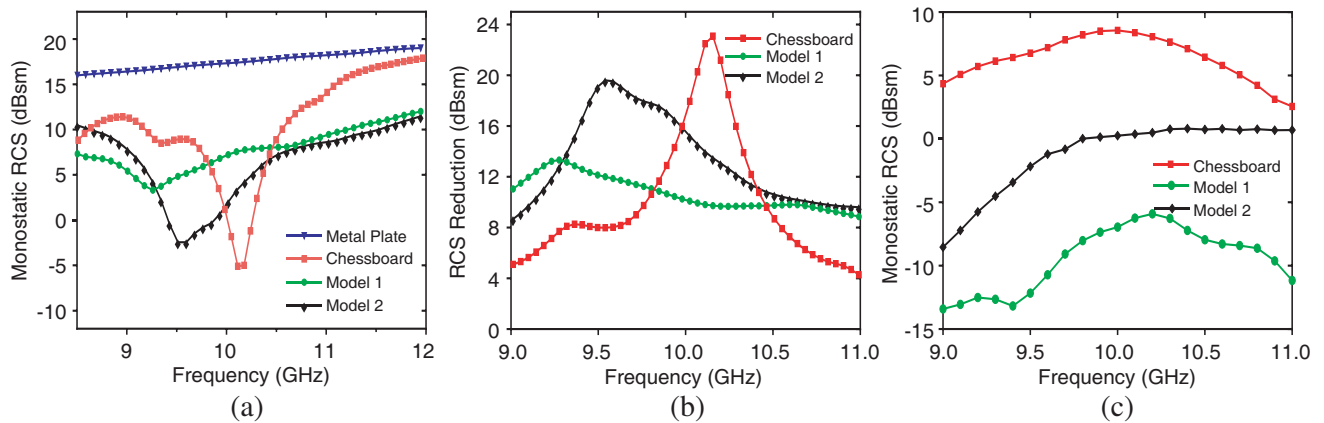


Figure 6. Broadband comparisons of (a), (b) monostatic RCS, RCS reduction at $(\theta = 0^\circ, \phi = 0^\circ)$, (c) RCS at $(\theta = 30^\circ, \phi = 45^\circ)$ to observe the performance of diagonal beams.

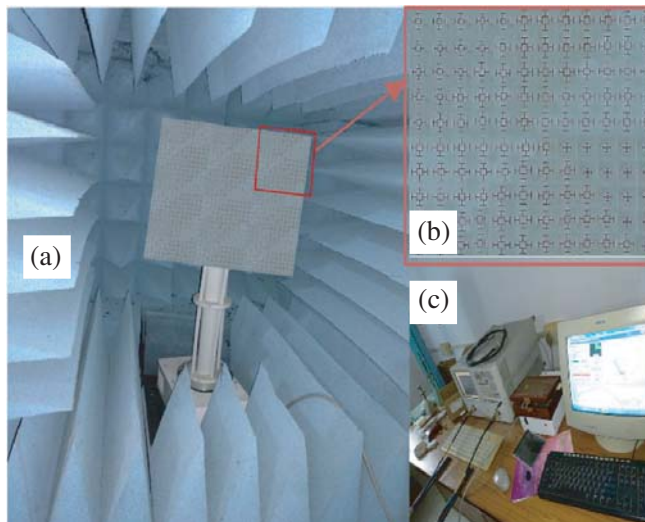


Figure 7. (a) The measurement setup, (b) model-2 prototype and (c) the control unit.

10 GHz. RCS versus frequency curve at $\varphi = 45^\circ$ and $\theta = \pm 30^\circ$ plane shown in Figure 6(c) clears the concept drawn from the 3D RCS pattern, and it shows demerit of chessboard surface which has four main beams at the diagonal plane. Also, model-1 has the minimum RCS because the reflected beams are situated on x -axis and y -axis, while the chessboard has a maximum reflection on this plane due to four diagonally reflected beams. Conclusively all the RCS results demonstrate that model-2 is most efficient among all three designed phase quantized surfaces which diffuse the incident beams towards all directions above the surface and reduce the maximum RCS dramatically due to the random distribution of phased grids inside the rectangular supercell.

Due to better RCS reduction performance among above-studied cases, we fabricate model-2 for experimental realization. A low-cost copper coated FR4 substrate is used in the dry-etching machine to prepare the prototype displayed in Figure 7(b). Due to limited experimental resources, only monostatic RCS for a normally incident waves is measured. We conduct measurements inside a mini-anechoic chamber shown in Figure 7(a) where the prototype is mounted on a vertical mast.

To measure the RCS we used Agilent two-port Vector Network Analyser (PNA N5230) with two standard gain X-band horn antennas. The distance between the target area and the antennas is maintained to 1 meter ($D > 20\lambda$) for better results, and the antennas are connected to the Tx and Rx ports of the VNA. At the first step, S_{21F} (frequency domain data) is recorded for the measurement chamber without the target and converted to time/distance domain using Fourier transform (S_{21T}). Similarly, S_{21T} is recorded with the target placed on the supporting mask (absorber sheets are used to cover the mast for better results). Based on the procedures described in [40] and the operation manual of equipment mentioned above, the following calculations are used to obtain the RCS of the PQS mode-2.

$$S_{21T} = 10 \log \frac{P_r}{P_t} \quad (4)$$

$$P_r = P_t 10^{\frac{S_{21T}}{10}} \quad (5)$$

$$\sigma = \frac{P_r}{P_t} [(4\pi)^3 R^4 / G_t G_r \lambda^2] \quad (6)$$

$$\sigma_{\text{target}} = \sigma_{\text{calib}} 10^{\left(\frac{S_{21T}(\text{target}) - S_{21T}(\text{calib})}{10}\right)} \quad (7)$$

Here,

P_t & P_r = Transmitted & received Power

G_t & G_r = Gain of transmitting and receiving antennas

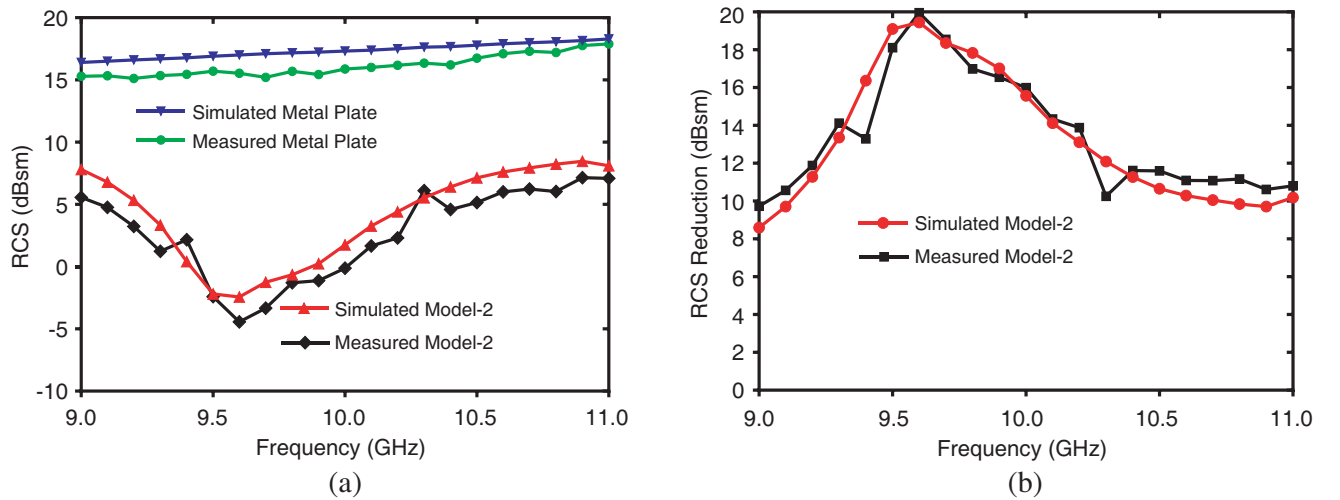


Figure 8. (a) Simulated and measured monostatic RCS comparisons of the PQS model-2 and a metallic plate of same dimensions, (b) RCS reduction for model-2 concerning the metallic plate.

R = Range between target and antenna

S_{21T} = Time domain transmission coefficient (calib and target stands for without and with the target)

σ = Radar Cross Section (RCS)

Measured monostatic RCS of PQS model-2 is compared with the simulated results in Figure 8(a) to strengthen the proposed model. Approximately 18%–20% measurement error is observed in both metal plate and PQS case. Figure 8(b) displays the simulated and measured RCS reductions for the PQS from which 10 dBsm reduction can be observed from 9 GHz to 11 GHz. We can also obtain more than 15 dBsm reduction within 9.5 GHz to 10 GHz. Since the meta-elements have the same reflection phase response up to 25° incident angle as studied in Figure 1 and have a symmetric geometry at xoy plane, the PQS will function correctly for y -polarized waves and can tolerate incident angle up to 25° . Based on the same arguments, PQS proposed in this paper can be used to stealth electrically large and asymptotically curved structures at X-band regime.

4. CONCLUSION

Summarizing the work, we propose a remodeled Jerusalem cross type meta-atom which is suitable to obtain quasi-linear 2π phase jump by variation of printed element size. A simple 3-bit phase quantization scheme is equipped for simplifying the distribution of phase in future applications. Manipulation of a normal incident and applications like splitting and focusing of the plane wave using PQS are tested using generalized laws of reflection. Two eight sector based supercell models are proposed and arranged in a 3×3 matrix to obtain bistatic RCS by numerical simulations. Results are compared with that of the conventional chessboard type surface designed using the same meta-element and copper plate. Model-1 redistributes the reflected beam along the x -axis and y -axis plane while model-2 gives the best results by diffusing the reflected beams throughout all directions. RCS reduction of 10 dBsm is observed from 9 GHz to 11 GHz in both models while chessboard surface behaves as a resonant surface. A fabricated prototype of model-2 is measured for backscattering RCS which provides a 15 dBsm reduction from 9.5 GHz to 10 GHz and considered as the best supercell model for ultrathin shielding application at X-band. Further, possible improvements can be made by improving the operating bandwidth of the meta-atoms and considering the conversion of polarization by using suitable meta-atoms.

ACKNOWLEDGMENT

The authors are thankful to the Department of Science and Technology, Govt. of India for financial support to Mr. R. Swain as INSPIRE Fellowship.

REFERENCES

1. Smith, D. R., J. B. Pendry, and M. C. Wiltshire, "Metamaterials and negative refractive index," *Science*, Vol. 305, No. 5685, 788–792, 2004.
2. Schurig, D., J. J. Mock, B. J. Justice, S. A. Cummer, J. B. Pendry, A. F. Starr, and D. R. Smith, "Metamaterial electromagnetic cloak at microwave frequencies," *Science*, Vol. 314, No. 5801, 977–980, 2006.
3. Shalaev, V. M., "Optical negative-index metamaterials," *Nature Photonics*, Vol. 1, No. 1, 41, 2007.
4. Shelby, R. A., D. R. Smith, and S. Schultz, "Experimental verification of a negative index of refraction," *Science*, Vol. 292, No. 5514, 77–79, 2001.
5. Pendry, J. B., D. Schurig, and D. R. Smith, "Controlling electromagnetic fields," *Science*, Vol. 312, No. 5781, 1780–1782, 2006.
6. Capasso, F., "Metasurfaces: From quantum cascade lasers to flat optics," *42nd International Conference on Infrared, Millimeter, and Terahertz Waves (IRMMW-THz)*, 1–3, IEEE, 2017.

7. Yu, N., P. Genevet, M. A. Kats, F. Aieta, J. P. Tetienne, F. Capasso, and Z. Gaburro, "Light propagation with phase discontinuities: Generalized laws of reflection and refraction," *Science*, Vol. 334, No. 6054, 333–337, 2011.
8. Aieta, F., P. Genevet, M. A. Kats, N. Yu, R. Blanchard, Z. Gaburro, and F. Capasso, "Aberration-free ultrathin flat lenses and axicons at telecom wavelengths based on plasmonic metasurfaces," *Nano Letters*, Vol. 12, No. 9, 4932–4936, 2012.
9. Yu, N. and F. Capasso, "Flat optics with designer metasurfaces," *Nature Materials*, Vol. 13, No. 2, 139, 2014.
10. Karimi, E., S. A. Schulz, I. D. Leon, H. Qassim, J. Upham, and R. W. Boyd, "Generating optical orbital angular momentum at visible wavelengths using a plasmonic metasurface," *Light: Science & Applications*, Vol. 3, No. 5, e167, 2014.
11. Ma, X., M. Pu, X. Li, C. Huang, Y. Wang, W. Pan, B. Zhao, J. Cui, C. Wang, and Z. Zhao, "A planar chiral meta-surface for optical vortex generation and focusing," *Scientific Reports*, Vol. 5, 10365, 2015.
12. Yu, S., L. Li, G. Shi, C. Zhu, X. Zhou, and Y. Shi, "Design, fabrication, and measurement of reflective metasurface for orbital angular momentum vortex wave in radio frequency domain," *Applied Physics Letters*, Vol. 108, No. 12, 121903, 2016.
13. Zhu, H. L., S. W. Cheung, K. L. Chung, and T. I. Yuk, "Linear-to-circular polarization conversion using metasurface," *IEEE Transactions on Antennas and Propagation*, Vol. 61, No. 9, 4615–4623, 2013.
14. Chen, H., J. Wang, H. Ma, S. Qu, Z. Xu, A. Zhang, M. Yan, and Y. Li, "Ultra-wideband polarization conversion metasurfaces based on multiple plasmon resonances," *Journal of Applied Physics*, Vol. 115, No. 15, 154504, 2014.
15. Estakhri, N. M. and A. Alù, "Ultra-thin unidirectional carpet cloak and wavefront reconstruction with graded metasurfaces," *IEEE Antennas and Wireless Propagation Letters*, Vol. 13, 1775–1778, 2014.
16. Ni, X., Z. J. Wong, M. Mrejen, Y. Wang, and X. Zhang, "An ultrathin invisibility skin cloak for visible light," *Science*, Vol. 349, No. 6254, 1310–1314, 2015.
17. Ni, X., A. V. Kildishev, and V. M. Shalaev, "Metasurface holograms for visible light," *Nature Communications*, Vol. 4, 2807, 2013.
18. Minatti, G., M. Faenzi, E. Martini, F. Caminita, P. De Vita, D. González-Ovejero, M. Sabbadini, and S. Maci, "Modulated metasurface antennas for space: Synthesis analysis and realizations," *IEEE Transactions on Antennas and Propagation*, Vol. 63, No. 4, 1288–1300, 2015.
19. Donda, K. D. and R. S. Hegde, "Rapid design of wide-area heterogeneous electromagnetic metasurfaces beyond the unit-cell approximation," *Progress In Electromagnetics Research M*, Vol. 60, 1–10, 2017.
20. Cui, T. J., M. Q. Qi, X. Wan, J. Zhao, and Q. Cheng, "Coding metamaterials, digital metamaterials and programmable metamaterials," *Light: Science & Applications*, Vol. 3, No. 10, e218, 2014.
21. Liu, S., T. J. Cui, Q. Xu, D. Bao, L. Du, X. Wan, W. X. Tang, C. Ouyang, X. Y. Zhou, and H. Yuan, "Anisotropic coding metamaterials and their powerful manipulation of differently polarized terahertz waves," *Light: Science & Applications*, Vol. 5, No. 5, e16076, 2016.
22. Chen, K., Y. Feng, Z. Yang, L. Cui, J. Zhao, B. Zhu, and T. Jiang, "Geometric phase coded metasurface: From polarization dependent directive electromagnetic wave scattering to diffusion-like scattering," *Scientific Reports*, Vol. 6, 35968, 2016.
23. Wan, X., M. Q. Qi, T. Y. Chen, and T. J. Cui, "Field-programmable beam reconfiguring based on digitally-controlled coding metasurface," *Scientific Reports*, Vol. 6, 20663, 2016.
24. Tymchenko, M., J. S. Gomez-Diaz, J. Lee, N. Nookala, M. A. Belkin, and A. Alù, "Gradient nonlinear pancharatnam-berry metasurfaces," *Physical Review Letters*, Vol. 115, No. 20, 207403, 2015.
25. Bahret, W. F., "The beginnings of stealth technology," *IEEE Transactions on Aerospace and Electronic Systems*, Vol. 29, No. 4, 1377–1385, 1993.

26. Park, M.-J., J. Choi, and S. S. Kim, "Wide bandwidth pyramidal absorbers of granular ferrite and carbonyl iron powders," *IEEE Transactions on Magnetics*, Vol. 36, No. 5, 3272–3274, 2000.
27. Li, M., S. Xiao, Y. Y. Bai, and B. Z. Wang, "An ultrathin and broadband radar absorber using resistive FSS," *IEEE Antennas and Wireless Propagation Letters*, Vol. 11, 748–751, 2012.
28. Chaudhury, B. and S. Chaturvedi, "Study and optimization of plasma-based radar cross section reduction using three-dimensional computations," *IEEE Transactions on Plasma Science*, Vol. 37, No. 11, 2116–2127, 2009.
29. Luukkonen, O., F. Costa, C. R. Simovski, A. Monorchio, and S. A. Tretyakov, "A thin electromagnetic absorber for wide incidence angles and both polarizations," *IEEE Transactions on Antennas and Propagation*, Vol. 57, No. 10, 3119–3125, 2009.
30. Watts, C. M., X. Liu, and W. J. Padilla, "Metamaterial electromagnetic wave absorbers," *Advanced Materials*, Vol. 24, No. 23, OP98–OP120, 2012.
31. Paquay, M., J. C. Iriarte, I. Ederra, R. Gonzalo, and P. de Maagt, "Thin AMC structure for radar cross-section reduction," *IEEE Transactions on Antennas and Propagation*, Vol. 55, No. 12, 3630–3638, 2007.
32. Simms, S. and V. Fusco, "Chessboard reflector for RCS reduction," *Electronics Letters*, Vol. 44, No. 4, 316–318, 2008.
33. Zhao, Y., X. Cao, J. Gao, and W. Li, "Broadband radar absorbing material based on orthogonal arrangement of CSRR etched artificial magnetic conductor," *Microwave and Optical Technology Letters*, Vol. 56, No. 1, 158–161, 2014.
34. Esmaeli, S. H. and S. H. Sedighy, "Wideband radar cross-section reduction by AMC," *Electronics Letters*, Vol. 52, No. 1, 70–71, 2015.
35. Mighani, M. and G. Dadashzadeh, "Broadband RCS reduction using a novel double layer chessboard AMC surface," *Electronics Letters*, Vol. 52, No. 14, 1253–1255, 2016.
36. Sun, H., C. Gu, X. Chen, Z. Li, L. Liu, B. Xu, and Z. Zhou, "Broadband and broad-angle polarization-independent metasurface for radar cross section reduction," *Scientific Reports*, Vol. 7, 40782, 2017.
37. Su, P., Y. Zhao, S. Jia, W. Shi, and H. Wang, "An ultra-wideband and polarization-independent metasurface for RCS reduction," *Scientific Reports*, Vol. 6, 20387, 2016.
38. Li, Q. Y., Y. C. Jiao, and G. Zhao, "A novel microstrip rectangular-patch/ring-combination reflectarray element and its application," *IEEE Antennas and Wireless Propagation Letters*, Vol. 8, 1119–1122, 2009.
39. Chen, W., C. A. Balanis, and C. R. Birtcher, "Checkerboard EBG surfaces for wideband radar cross section reduction," *IEEE Transactions on Antennas and Propagation*, Vol. 63, No. 6, 2636–2645, 2015.
40. Knott, E. F., *Radar Cross Section Measurements*, Springer, US, 1993.